

Journal of Materials Chemistry A

Accepted Manuscript



This is an *Accepted Manuscript*, which has been through the Royal Society of Chemistry peer review process and has been accepted for publication.

Accepted Manuscripts are published online shortly after acceptance, before technical editing, formatting and proof reading. Using this free service, authors can make their results available to the community, in citable form, before we publish the edited article. We will replace this *Accepted Manuscript* with the edited and formatted *Advance Article* as soon as it is available.

You can find more information about *Accepted Manuscripts* in the [Information for Authors](#).

Please note that technical editing may introduce minor changes to the text and/or graphics, which may alter content. The journal's standard [Terms & Conditions](#) and the [Ethical guidelines](#) still apply. In no event shall the Royal Society of Chemistry be held responsible for any errors or omissions in this *Accepted Manuscript* or any consequences arising from the use of any information it contains.

Hierarchically mesoporous carbon nanopetals based electrodes for flexible supercapacitors with super-long cyclic stability

Jayesh Cherusseri^a and Kamal K. Kar^{a,b*}

^aAdvanced Nanoengineering Materials Laboratory, Materials Science Programme, Indian Institute of Technology, Kanpur, Uttar Pradesh-208016, India.

^bAdvanced Nanoengineering Materials Laboratory, Department of Mechanical Engineering, Indian Institute of Technology, Kanpur, Uttar Pradesh-208016, India.

*Corresponding author. Tel: +91-512-2597687, E-mail: kamalkk@iitk.ac.in (Kamal K. Kar)

Abstract

Hierarchically mesoporous carbon nanopetals (CNPs) are synthesized on unidirectional carbon fiber (UCF) by catalytic chemical vapour deposition. The CNPs synthesized on UCF (CNPs/UCF) are further used as electrode-cum-current collectors for fabricating a flexible supercapacitor. Highly bendable and electrically conductive UCFs are used both as substrate for the growth of CNPs as well as the current collectors for the supercapacitor and no other separate current collectors are used in this study. The CNPs/UCF hybrids are characterized by transmission electron microscopy, scanning electron microscopy, Fourier transform infrared spectroscopy, X-ray photoelectron spectroscopy, Raman spectroscopy, and Brunauer-Emmett-Teller surface area measurement. The electrochemical performance of the CNPs/UCF supercapacitor is examined by electrochemical impedance spectroscopy, cyclic voltammetry, and galvanostatic charge/discharge measurement. The mesoporous CNPs/UCF hybrid electrodes based symmetric supercapacitor is highly bendable and the performance of the supercapacitor is unaltered even at smaller bending angles. The CNPs/UCF supercapacitor exhibits a high gravimetric capacitance of 154 F g^{-1} with a high specific power density of 32 kW kg^{-1} at a current density of 16.66 mA cm^{-2} . The enhanced supercapacitive performance of CNPs/UCF supercapacitor is mainly due to the mesoporous electrode nanostructure as well as due to the presence of oxygen-containing functional groups on the surface of CNPs/UCF hybrids. The CNPs/UCF supercapacitor possesses a super-long cyclic stability of more than 28900 cycles. The supercapacitive performances of CNPs/UCF supercapacitor are comparable to that of those utilizing other carbon nanomaterials based electrodes.

1. Introduction

Increasing energy crisis in the world has boosted the development of various efficient energy storage technologies. Sustainability and renewability are the two major concerns in the

energy research. Due to the intermittent nature of various renewable energy conversion technologies, the energy storage technologies become inevitable part and hence the investment on the research and development of energy storage technologies such as batteries and supercapacitors are increasing nowadays. A primary focus is on the development of supercapacitors since these fascinating devices can deliver extremely high power when compared to that of batteries. The development of various types of supercapacitors namely, electrochemical double layer capacitors (EDLCs), pseudocapacitors (otherwise known as redox capacitors), and hybrid capacitors have changed the faces of conventional energy storage technologies with their superior electrochemical performances. Supercapacitors exhibit high power densities, high rate charge/discharge capabilities, long cycle life and safe operation.¹⁻³ EDLCs store charges by the formation of electrochemical double layer at the electrode/electrolyte interface whereas pseudocapacitors make use of electron transfer reactions such as *Faradic*-reactions for their charge storage. Carbon nanomaterials based electrodes are much preferred candidates for EDLCs due to their unique properties such as good electronic conductivity, extremely large surface area, low density with high mechanical strength, good chemical stability, etc.⁴⁻⁸ EDLCs exhibit high power densities with highly reversible charge/discharge profiles as there is no permanent change is occurred for the electro-active materials. For pseudocapacitors, transition metal oxides^{9,10} and electronically conducting polymers^{11,12} are the choices and they possess much higher capacitance and energy density while compared to that of EDLCs.

Flexible supercapacitor electrodes have achieved much demand nowadays due to their easy incorporation with various advanced flexible electronic devices. The flexible electronic systems including portable electronic papers, roll-up and bendable displays, wearable multimedia, etc., require very thin and flexible devices to supply the power.¹³⁻¹⁵ The easiness in the integration of supercapacitors with many of the primary energy conversion

technologies such as polymer electrolyte membrane fuel cells, thermoelectric generators, photovoltaic cells, etc. is their other technological advantage. Carbon nanomaterials such as carbon nanotubes (CNTs) and graphene have achieved much importance in the preparation of flexible electrodes for supercapacitors.¹⁶⁻¹⁹ Supercapacitor electrodes with high mechanical strength and bending strength are mandatory for flexible energy storage applications.

The synthesis of flexible electrodes is a tedious task as the performance of the supercapacitor device shouldn't be altered during its operation at its severe bending. The preparation of flexible supercapacitor electrode includes spray-coating of carbon nanomaterials over flexible, non-conductive substrates such as cellulose paper and plastic films²⁰⁻²³ and conductive metallic substrates.^{24,25} In the case of supercapacitors with planar electrode architecture, the effective utilization of specific surface area of the electrodes is minimal and it inhibits the diffusion of electrolyte to the electrode, which eventually deteriorates the performance of the supercapacitor. Another viable method of preparing flexible supercapacitor electrode is by electrochemical deposition procedures whereby a control over the electrode material coating can be achieved either in terms of coating thickness or in terms of mass loading. Electrochemical deposition includes the deposition of electro-active materials on to electrically conductive substrates such as metal plates with the aid of electricity.²⁶⁻²⁹ These substrates are further used as secondary current collectors for the supercapacitor during its fabrication. The drawbacks of electrochemical deposition include (i) it leads to the agglomeration of electro-active materials on the substrate and (ii) the supercapacitor device become highly massive due to the usage of heavy current collectors. It is obvious that an agglomerated electrode architecture can worsens the performance of the supercapacitor. A best solution to these problems is to synthesize electro-active materials on lightweight and electrically conductive substrates and subsequently use these as electrode-cum-current collectors for supercapacitors.

Fibrous flexible supercapacitor electrodes are attaining much importance in the area of wearable electronics and various types of fiber materials decorated with carbon nanomaterials are effectively utilized as flexible fiber electrodes for supercapacitors.³⁰⁻³³ Examples for fiber materials exploited as the substrates for manufacturing fibrous and flexible supercapacitor electrodes are Kevlar fiber,³⁴ metal fiber,³⁵ carbon fiber,³⁶ CNT fibers,³⁷ graphene fiber,³⁸ etc. Among these fibrous materials, carbon fibers based flexible electrodes are efficient candidates for synthesizing flexible supercapacitors as they possess good mechanical properties, good electrical conductivity, and outstanding bendability.^{39,40} But the processing of carbon fibers based flexible electrodes requires sophisticated machineries and hence the cost of such supercapacitors obviously be very high. Hence it is required to develop cost-effective fibrous electrodes for flexible supercapacitors. In the present study, we report the novel synthesis of unique hierarchically mesoporous carbon nanopetals (CNPs) on unidirectional carbon fiber (UCF) by catalytic chemical vapour deposition (CVD). The CNPs grown on UCF (CNPs/UCF) is further used as electrode-cum-current collector for fabricating flexible supercapacitors. To the best of our knowledge, this is the first time report of synthesizing CNPs/UCF hybrids and subsequently used as electrode-cum-current collector in supercapacitors. Herein, no separate current collectors are used whereas the catalyst non-coated portions of the UCFs were used as current collectors for fabricating the supercapacitors. The novel CNPs/UCF hybrid electrode-cum-current collector is highly bendable and helps in reducing the mass of supercapacitor as compared to that of those utilizing metallic current collectors.

2. Experimental Section

Materials

Polyacrylonitrile based UCFs (specific density $\sim 1.8 \text{ g cm}^{-3}$, tensile strength $\sim 1900\text{-}2750$ MPa, diameter $\sim 8 \text{ }\mu\text{m}$) were received from M/S Fortafil Industries Inc., U.K. Nickel sulphate

hexahydrate ($\text{NiSO}_4 \cdot 6\text{H}_2\text{O}$, 99%), ammonium chloride (NH_4Cl , 99%), trisodium citrate ($\text{Na}_3\text{C}_6\text{H}_5\text{O}_7 \cdot 2\text{H}_2\text{O}$, 98%), liquor ammonia (NH_3 , 25%) were obtained from M/S Qualigens Fine Chemicals, India. Sodium hypophosphite ($\text{NaH}_2\text{PO}_2 \cdot \text{H}_2\text{O}$, 99%) and potassium hydroxide (KOH , 99%) were obtained from M/S Loba Chemie Pvt. Ltd., India. Thiophene ($\text{C}_4\text{H}_4\text{S}$) was supplied by M/S Sigma Aldrich, India.

Synthesis of CNPs

UCFs having individual fiber diameter of $\sim 8 \mu\text{m}$, were used as the substrate to grow CNPs by catalytic CVD. Initially, nickel was coated on UCFs by electroless coating.⁴¹ The electroless coating bath was consisted of nickel sulphate hexahydrate (35 g l^{-1}), sodium hypophosphite (12 g l^{-1}), ammonium chloride (45 g l^{-1}), trisodium citrate (25 g l^{-1}), and liquor ammonia (3 ml). Here, the nickel sulphate hexahydrate was functioned as the source of nickel ions and sodium hypophosphite as reducing agent, ammonium chloride as complexing agent, and trisodium citrate as stabiliser for the electroless coating bath. Liquor ammonia was used to control the pH of the coating bath. Initially, the UCFs were dipped inside the electroless coating bath kept at $85 \text{ }^\circ\text{C}$ under constant stirring for a period of 10 min, rinsed severally with ethanol and de-ionized water and then subsequently dried at $85 \text{ }^\circ\text{C}$ for 24 h. The electroless nickel-coated UCF strands were further oxidized by annealing them at $550 \text{ }^\circ\text{C}$ in an air-bed reactor for a period of 30 min. These oxidized, nickel-coated UCFs were used as substrate for the synthesis of CNPs by catalytic CVD thereafter. During the catalytic CVD process, the oxidized nickel-coated UCFs were heated to $500 \text{ }^\circ\text{C}$ in a horizontal quartz furnace (1.12 m length with 105 mm diameter) under a continuous N_2 flow (200 ml min^{-1}). In order to prevent the further formation of oxides on the nickel particles, H_2 was introduced at a flow rate of 100 ml min^{-1} for 15 min. The temperature was further increased to $700 \text{ }^\circ\text{C}$ and acetylene was introduced at a flow rate of 90 ml min^{-1} for 15 min while keeping the N_2 flow fixed at 200 ml min^{-1} throughout and thiophene was introduced simultaneously by heating the thiophene

was used as the electrolyte. In the as fabricated supercapacitor cell, the nickel uncoated portion of CNPs/UCF strands were used as current collecting leads and no separate current collectors were used in this study.

Material Characterizations

The microstructure and surface topography of the CNPs/UCF hybrids were studied using a scanning electron microscope (SEM; Carl Zeiss EVO MA 15) and transmission electron microscope (TEM; FEI Technai G2 12 Twin TEM 120 kV). Energy dispersive X-ray analysis was carried out by EDS spectrometer (EDS; INCA Penta FETx3, Oxford Instruments, U.K.), attached to SEM (Carl Zeiss, EVO 50, Oberkochen, Germany) to know the elemental composition of oxidized, nickel-coated UCFs. The thicknesses of the supercapacitor electrodes and the supercapacitor cell were measured by using a thickness gauge (S. C. Dey & Co., India). Raman spectra of the CNPs/UCF hybrids were analyzed with the help of LabRam Micro Raman Spectrometer (Jobin-Yuon HR 800 UV) by using a He-Ne (632.7 nm) laser excitation source. Fourier transform infrared spectroscopy (FT-IR) experiments were performed by using infrared spectrometer (Perkin Elmer Spectrum 1) at the frequency range (4000–400) cm^{-1} in transmission mode spectrum. X-ray photoelectron spectroscope (XPS; PHI 5000 Versa Probe II, FEI Inc.) was employed to probe the chemical state of CNPs/UCF hybrids. The high-resolution XPS spectra corresponding to C 1s and O 1s peaks of CNPs/UCF hybrids were analyzed by using the XPS Peak version 4.1 program, where Shirley-typed background and Gaussian-Lorentzian distributions are used to fit the baselines and the XPS peaks, respectively. The N_2 sorption surface area measurement of CNPs/UCF hybrids was performed with a surface area analyzer (Quantachrome Instruments Version 3.01, U.S.A.). The mass of CNPs was measured by using a microbalance with readability of 1 μg (XP 6, Mettler Toledo).

Testing of CNPs/UCF Supercapacitor

A symmetric two-electrode cell configuration was used to check the performance of the CNPs/UCF supercapacitor. Cyclic voltammetry (CV), electrochemical impedance spectroscopy and galvanostatic charge/discharge measurements were used to investigate the electrochemical performances of the supercapacitor cells. The CV and galvanostatic charge/discharge measurements were carried out with the help of an electrochemical testing station (CHI 608D, CH Instruments, U.S.A.). The CV measurements were performed within a potential window of 0 to 1 V at different scan rates. The impedance spectroscopic measurement was carried out with an electrochemical analyzer (CHI 660C, CH Instruments, U.S.A.) within a frequency range of $10^5 - 0.02$ Hz. All the calculations related to the supercapacitor cell testing are discussed in the electronic supplementary information (ESI).

3. Results and discussion

The SEM image of nickel-coated UCFs (**Figure S2**) reveals that the nickel nanoparticles are uniformly coated over the UCFs. The electroless coating method has helped to obtain a uniformly distributed catalyst over the substrate for the growth of CNPs. The air-oxidation at 550 °C has enabled the oxidation of nickel-coated UCF substrate, which can be verified from the EDS spectra (**Figure S3**). From the EDS spectra, it is clear that only a small amount of nickel is coated over the UCF substrates (1.4 at%). These oxidized, nickel-coated UCF substrates support the growth of CNPs in a catalyst mediated growth mechanism. The synthesis of CNPs on UCF with high density is achieved due to the oxidation treatment and also the use of thiophene. The processing was repeated (i) without oxidizing the nickel-coated UCFs and using thiophene and (ii) using oxidized, nickel-coated UCFs and without using thiophene; in both the cases the growth of CNPs is not achieved. Hence it can be say that the novel hierarchical CNPs are grown on UCF through defect induced growth mechanisms whereby nickel oxide act as the nucleation centre for the growth of CNP and sulphur

functions as the defect inducing impurity during the growth. A growth mechanism for CNPs is proposed and the proposed model is shown in **Fig. 1B**. CVD growth of CNPs consists of four sequential processes, mass transport and reactions in the gas phase, dissociative absorption of the carbon atoms on the nickel oxide surface, diffusion of the resulting carbon atoms over its surface, and finally precipitation of carbon atoms from the nickel oxide to form the growing nanopetal. It is also expected similar to the growth of CNTs that the growth rate of nanopetals on nickel oxide is limited by the diffusion of carbon through the nickel oxide nanoparticle. **Fig. 2A-D** show the SEM images of CNPs grown on UCF, at different magnifications. From these images, it is clear that petal-like carbon nanostructures with nanometer thickness (henceforth it is termed as “CNPs”) is grown on UCFs with high density. From the SEM images, the height of CNPs grown on UCF lies in between 5-12 μm with an average thickness of 60 nm. The TEM images of the tip portions of the CNPs are given in **Fig. 2E-G**. From the TEM images, it is evident that the thickness of CNPs at its central region is higher than that of their edges, which gives mechanical strength to the CNPs in order to grow vertically upwards on the UCF. And also, the CNPs exhibit three dimensional porous architecture (**Fig. 2G**), which is very helpful for the rapid charging/discharging of the supercapacitor. The selected area electron diffraction (SAED) pattern of CNPs is depicted in **Fig. 2H**, from which it is clear that the CNPs are not crystalline.

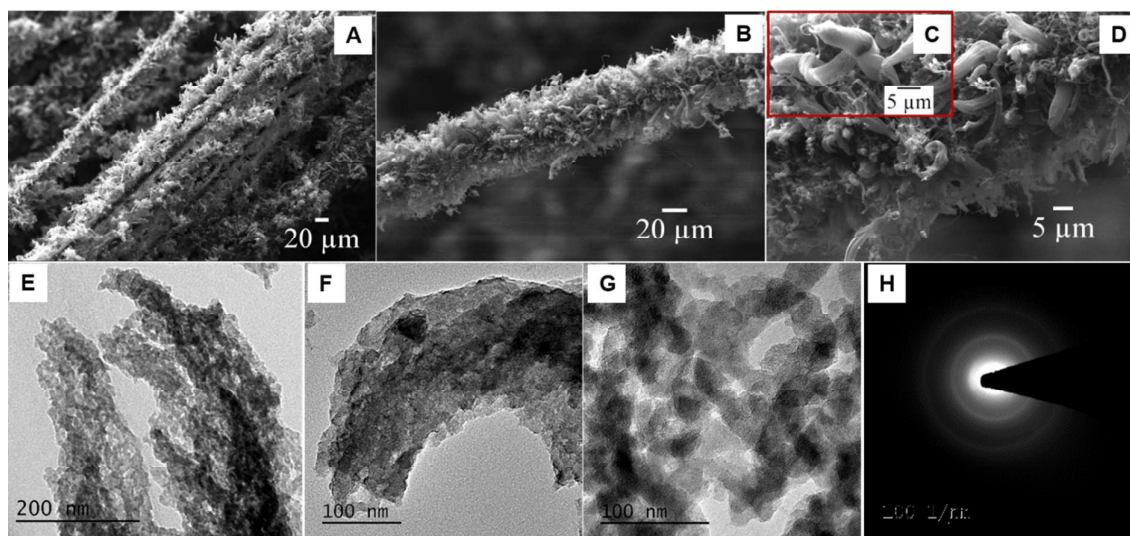


Fig. 2. (A-D) SEM images and (E-G) TEM images of CNPs grown on UCFs at different magnifications; (H) Selected area electron diffraction (SAED) pattern of CNPs.

The fingerprint Raman spectra of CNPs/UCF hybrids is shown in **Fig. 3**. The spectra contain two characteristic peaks that lie at ~ 1320 and ~ 1595 cm^{-1} correspond to D- and G-band of graphitic carbon, respectively. The D-band represents defects and lattice distortions and a highly intense D-band can be seen in the Raman spectra of CNPs. The I_D/I_G ratio of CNPs/UCF hybrids is 0.96, this lower value indicates that the CNPs possess a sp^2 -hybridized dominated carbon structure with defects, which is in good agreement with the XPS results, which will be discussed later.⁴²

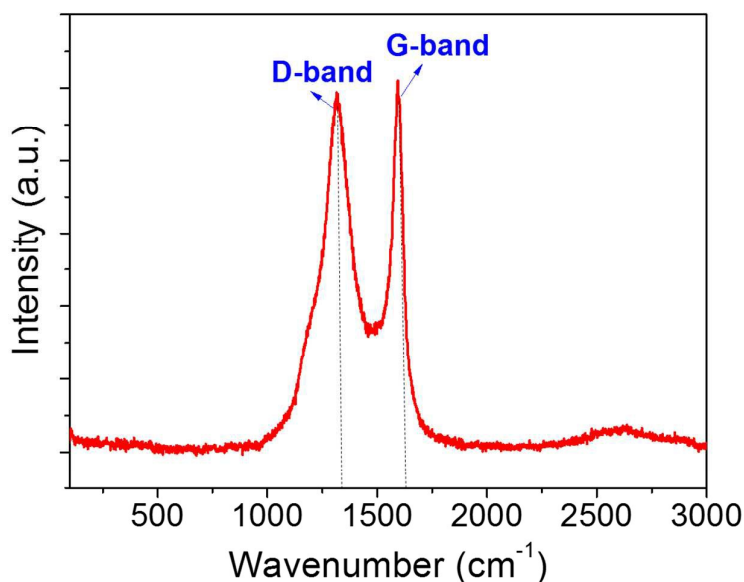


Fig. 3. Fingerprint Raman spectra of CNPs grown on UCFs.

Investigations of the presence of functional groups on the surface of CNPs/UCF hybrids have been performed using FT-IR analysis. **Fig. 4** shows the FT-IR spectra of CNPs/UCF hybrids. In this spectra, the band at 3433 cm^{-1} as a broad and intense signal can be assigned to the O-H stretches due to the vibrations of intercalated water molecules. The peak located at 1616 cm^{-1} can be assigned not only to the vibrations of adsorbed water molecules but also the skeletal vibration of C=C from un-oxidized sp^2 CC bonds. Band at 1242 cm^{-1} is corresponds to C-OH stretching, a low intensive peak at 1040 cm^{-1} is corresponds to C-O stretching and peak at 1126 cm^{-1} is corresponds to C-O-C symmetric stretching.^{43,44} From the FT-IR spectra, it is clear that various oxygen-containing functional groups are attached with the surfaces of CNPs/UCF hybrids.

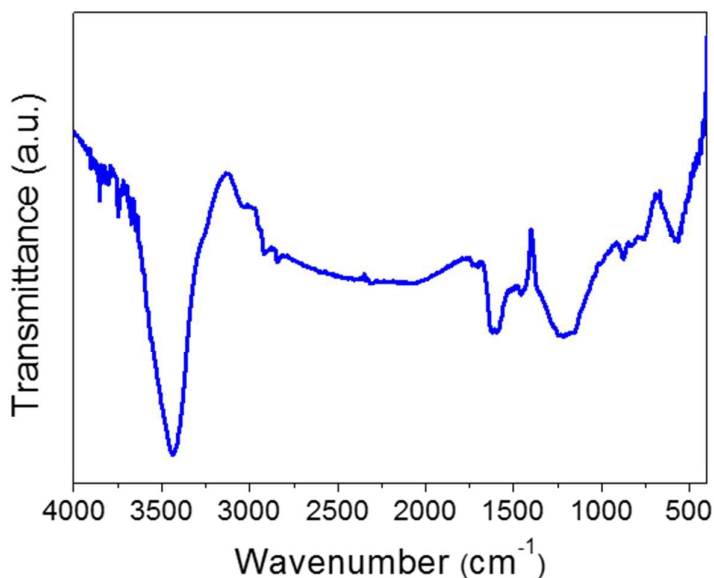


Fig. 4. FT-IR spectra of CNPs grown on UCFs.

In order to examine the chemical bonding states of the synthesized CNPs, XPS measurements were performed. **Fig. 5A** shows the XPS survey scans of CNPs/UCF hybrids, which clearly shows the presence of carbon and oxygen. **Fig. 5B and C** represent the high-resolution XPS C 1s and O 1s spectra of CNPs/UCF hybrids, respectively. The three components of C 1s peaks in **Fig. 5B** correspond to the sp^2 -hybridized carbons (at 283.78 eV), the sp^3 -hybridized carbons (at 284.52 eV), and carbon atoms singly bonded to oxygen (at 288.21 eV).⁴⁵⁻⁴⁷ As sp^3 and sp^2 components can be effectively assessed by the XPS analysis, it is to be noted here that the chemical shifts of the C 1s spectra due to sp^3 and sp^2 do not bear a direct relationship with the matrix.⁴⁸ The intensity of the binding energy is linearly proportional to the fraction of sp^3 and sp^2 bonds.⁴⁹ The XPS C 1s peak at 283.78 eV can be assigned to the graphitic carbons and 284.52 eV can be assigned to the defective carbons. The O 1s spectra of CNPs/UCF hybrids (**Fig. 5C**) are deconvoluted into four peaks corresponding to C=O (at 530.64 eV), C-O-C (at 531.6 eV), C-O (532.66 eV), and chemisorbed oxygen (535 eV).^{47,50,51} As aforementioned, Raman spectra (**Fig. 3**) clearly shows that the synthesized CNPs are defective and is in good agreement with the XPS results too.

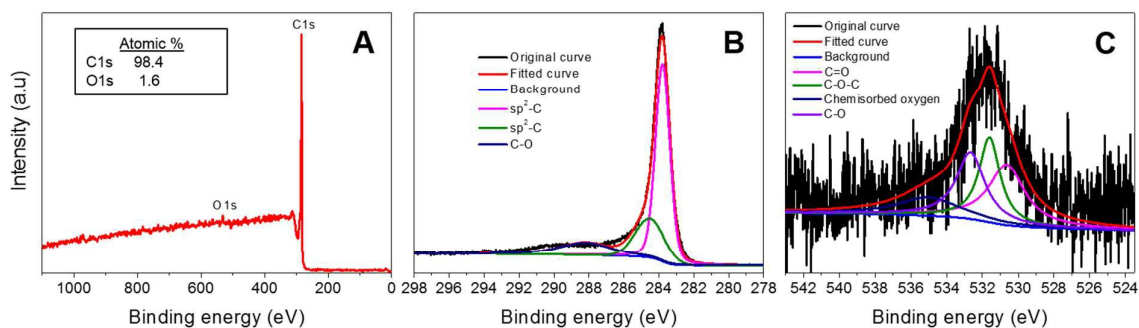


Fig. 5. XPS survey spectra (A), C 1s spectra (B), and O 1s spectra (C) of CNPs/UCF hybrids.

Brunauer-Emmett-Teller (BET) surface area measurement is carried out in order to examine the surface area of the synthesized CNPs. The CNPs/UCF hybrids possess a BET surface area of $256.4 \text{ m}^2 \text{ g}^{-1}$. The N_2 sorption isotherms shown in **Fig. 6A** indicate that the type of sorption process is of type IV in nature, which demonstrates the capillary condensation of gas within the tiny capillary pores of the CNPs/UCF hybrids at pressures below the saturation pressure of N_2 gas.⁵² Type IV isotherms (**Fig. 6A**) confirms that the CNPs/UCF hybrids are having a mesoporous structure and hence with high specific surface area, which is very beneficial to the enhanced electrochemical energy storage as the surface area is directly proportional to the capacitance of supercapacitor electrodes.⁵³ The supercapacitors with large electrode specific surface area are found to deliver high specific capacitances.⁵⁴ The total pore volume of CNPs/UCF hybrids is $0.541 \text{ cm}^3 \text{ g}^{-1}$ for pores smaller than 1596.9 \AA (radius) at $P/P_0 = 0.994$. The open pore structure is effectively utilized by the N_2 gas molecules during the sorption process. The average pore radius of CNPs/UCF hybrids is calculated from the Barrett-Joyner-Halenda (BJH) pore-size distribution curve (**Fig. 6B**) and is found to be 4.2 nm . It is well understood that the pore-sizes in the mesopore range are required to attain the maximum capacitance in EDLCs.⁵⁵ Since the majority of pores within the CNPs/UCF hybrids are the three dimensional mesopores and hence an enhanced electrochemical performance of the supercapacitor can be expected. From all the above analyses, mesoporous CNPs/UCF electrode-cum-current collectors are beneficial to

use in supercapacitors since it possess large surface area with mesoporous structure, lightweight, etc. Since we have used highly bendable UCFs as current collectors, high flexibility is achieved for the supercapacitor assembled with CNPs/UCF hybrids.

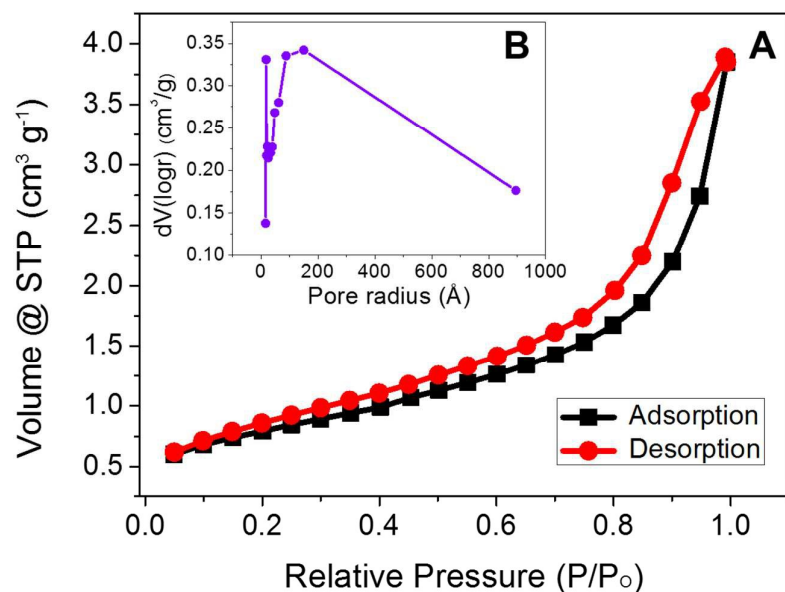


Fig. 6. (A) N₂ sorption isotherms, and (B) BJH pore-size distribution curve of CNPs/UCF hybrids.

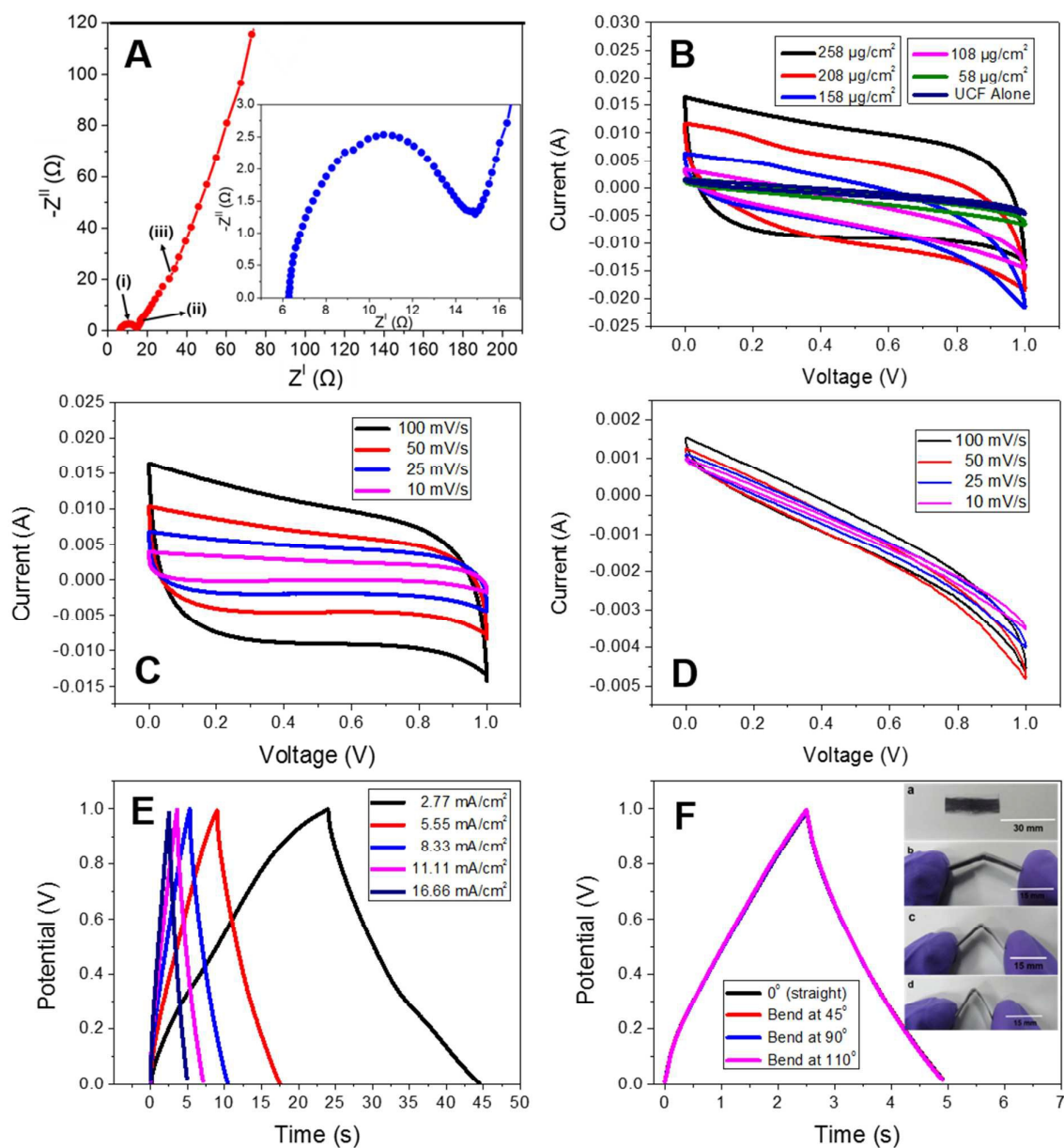


Fig. 7. (A) Nyquist plot (inset shows the magnified high-frequency regions), (B) CV curves at different CNPs loading densities and (C) CV curves at various scan rates with a CNPs loading density of $258 \mu\text{g cm}^{-2}$ of the CNPs/UCF supercapacitor; (D) CV curves of UCF supercapacitor at different scan rates; (E) galvanostatic charge/discharge curves at different current densities and (F) galvanostatic charge/discharge curves at different bending angles of the CNPs/UCF supercapacitor [Inset (F): digital images of the CNPs/UCF supercapacitor bend at 0° (a), 45° (b), 90° (c), and 110° (d)].

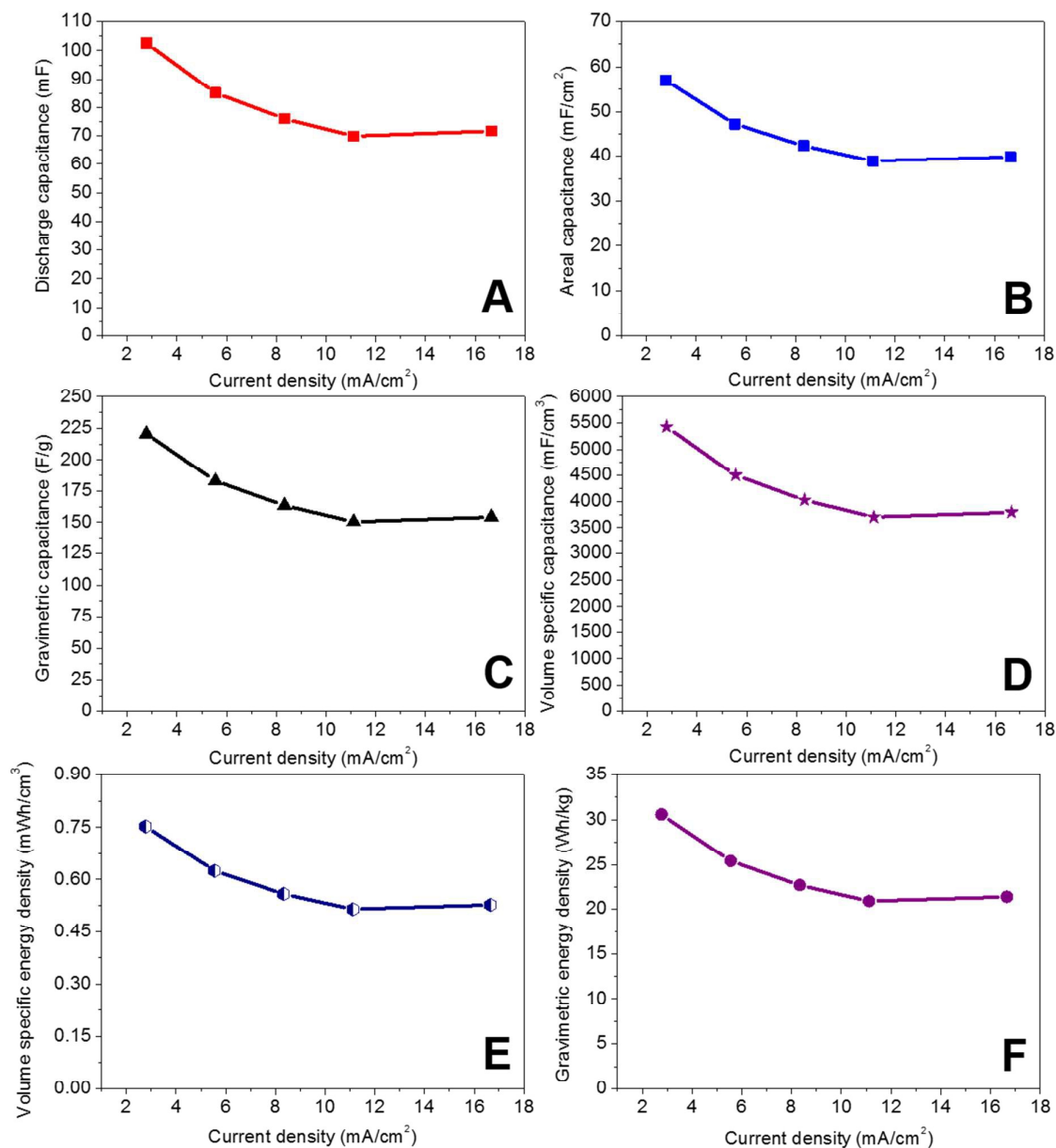


Fig. 8. Plots of discharge capacitance (A), areal capacitance (B), gravimetric capacitance (C), volume specific capacitance (D), volume specific energy density (E), and gravimetric energy density (F) at different current densities of the CNPs/UCF supercapacitor cell.

The electrochemical impedance spectra, represented by Nyquist plot of CNPs/UCF supercapacitor cell is shown in **Fig. 7A** and inset shows the magnified high-frequency regions. The plot consists of three segments: a semicircle in the high frequency region, a

Warburg line with a slope of approximately 45° in the middle frequency region and a vertical straight line in the lower frequency region. The first segment [denominated as (i) in **Fig. 7A**] represents the resistive nature of the supercapacitor cell. From the inset of **Fig. 7A**, it is clear that CNPs/UCF supercapacitor cell experience a bulk electrolyte resistance, R_b of $\sim 6.2 \Omega$. A lower value of R_b indicates high ionic conductivity exhibited by the CNPs/UCF hybrid electrodes and it may be due to the presence of some graphitic carbon components (CNPs and UCFs) within the hybrids. A conductivity of $9.31 \times 10^{-3} \text{ S cm}^{-1}$ is obtained for the CNPs/UCF hybrid electrodes, which indicates an enhanced ion diffusion through the three dimensional mesopores during the rapid charging/discharging process. The second segment [denominated as (ii) in **Fig. 7A**] represents the combined resistive and capacitive behaviour of the supercapacitor cell, and the third segment [denominated as (iii) in **Fig. 7A**] represents the capacitive behaviour of the supercapacitor cell. At lower frequency regions, the nearly vertical straight line shows the good capacitive behaviour of the CNPs/UCF supercapacitor. In order to understand the typical $I - E$ characteristics of the CNPs/UCF supercapacitor, a two-electrode cell cyclic voltammetry (CV) study has been carried out. **Fig. 7B** represents the CV curves scanned at different loading densities of CNPs in the CNPs/UCF hybrid electrodes at a constant scan rate of 100 mV s^{-1} . The different CNPs loading densities opted are 258, 208, 158, 108, and $58 \mu\text{g cm}^{-2}$. At higher loading densities, the CV curves appeared with high encircled areas. It is obvious that when the CNPs loading is decreased, the electrochemical activity of the electrodes is diminished. At a small CNPs loading density of $58 \mu\text{g cm}^{-2}$, the CV curve with a reduced encircled area is achieved and for pristine UCF (i.e., at zero loading of CNPs), CV curve with very low encircled area is obtained. At an optimal content of $258 \mu\text{g cm}^{-2}$ of CNPs in the CNPs/UCF hybrid electrodes is found to exhibit excellent electrochemical performance and hence this loading density was selected for the further electrochemical testing of the supercapacitor cell. The CV curves of CNPs/UCF

supercapacitor scanned at a CNP loading density of $258 \mu\text{g cm}^{-2}$ at various scan rates are shown in **Fig. 7C**. The CV curves displayed a nearly rectangular shape, indicating an efficient electrochemical double layer charge storage possess by the CNPs/UCF hybrid electrodes by imparting good charge propagation through the electrode-cum-current collectors. In order to show the electrochemical behaviours of pristine UCF supercapacitor, two-electrode cell CV study has been carried out for the same at different scan rates and the corresponding CV curves are depicted in **Fig. 7D**. It is clear from **Fig. 7D** that there is only negligible contribution on the charge storage possess by the pristine UCFs. The rate performance of CNPs/UCF hybrid electrodes is also evaluated by galvanostatic charging/discharging at different current densities. For this measurement, the CNPs/UCF hybrid electrodes with a CNP loading density of $258 \mu\text{g cm}^{-2}$ is used and the various current densities opted are 2.77, 5.55, 8.33, 11.11, and 16.66 mA cm^{-2} . The galvanostatic charge/discharge curves of the CNPs/UCF supercapacitor at different current densities are shown in **Fig. 7E**. From this figure, it can be seen that the CNPs/UCF supercapacitor can be charged with a high current density of 16.66 mA cm^{-2} , without affecting the charge/discharge profiles. The CNPs/UCF supercapacitor exhibits a high discharge capacitance of 102.6 mF at a current density of 2.77 mA cm^{-2} and a smaller value of 69.9 mF is obtained at a current density of 11.11 mA cm^{-2} . Although not a significant variation, a slight increase in the discharge capacitance (1.8 mF) is observed when the supercapacitor is charged at a comparatively high current density of 16.66 mA cm^{-2} . This is possibly due to the orientation of pores and/or CNPs in the direction of movement of electrolyte ions thereby improving the conductivity of CNPs accelerating its charge transfer during the discharge process at higher current densities.⁵⁶ A similar kind of variation can be seen in the case of areal, gravimetric and volume specific capacitances too. The variations in the discharge capacitance with respect to varying current densities are shown in **Fig. 8A**. An areal capacitance of 57 mF cm^{-2} is achieved at a lower current density

of 2.77 mA cm^{-2} and this value is decreased to 39.8 mF cm^{-2} at a current density of 16.66 mA cm^{-2} . The variations in the areal capacitance at different current densities are shown in **Fig. 8B**. The CNPs/UCF supercapacitor exhibits high gravimetric capacitances of 220 and 154 F/g at current densities of 2.77 and 16.66 mA cm^{-2} , respectively and the variations in the gravimetric capacitance with respect to varying current densities are plotted in **Fig. 8C**. These values are comparatively higher for the supercapacitors manufactured with pristine CNTs and graphene electrodes. **Table S1** compares the electrochemical performance of various supercapacitors utilizing carbon nanomaterials based electrodes. Volumetric capacitances of 1096 and 766 mF cm^{-3} are achieved by the CNPs/UCF supercapacitor at current densities of 2.77 and 16.66 mA cm^{-2} , respectively. The variations in the volumetric capacitance at different current densities are plotted in **Figure S4**. A high volume specific capacitance of 5428 mF cm^{-3} is achieved by the CNPs/UCF supercapacitor at a lower current density of 2.77 mA cm^{-2} . The volume specific capacitance of CNPs/UCF supercapacitor in the present study is the highest among the CFs based supercapacitors reported earlier.^{39,40} This high value is attributed to the large specific surface area and the mesoporous structure of CNPs/UCF hybrid electrodes as well as the presence of oxygen-containing surface functional groups attached with the CNPs/UCF hybrids. It is clear from the BET surface area analysis (**Fig. 6**) that the average pore-size of CNPs/UCF hybrids is mainly distributed around 4.2 nm and it favors fast ion-diffusion during the rapid charge/discharge process. The pseudo-*Faradic* charge storage exhibited by the oxygen-containing functional groups has contributed to the total capacitance of the CNPs/UCF supercapacitor to a great extent. The enhanced redox behaviour of carbon nanomaterials due to the presence of oxygen atoms at the edges of graphene layers is reported earlier.⁵⁷ Carbons have great ability to catalyze charge transfer reactions between the redox moieties present on them. During the redox reactions, the carbon surface is able to donate or withdraw electrons from/to radicals or ion-radicals present on the

carbon surface.⁵⁸ The presence of various oxygen-containing groups on the surface of CNPs/UCF hybrids is evident from the FT-IR spectra (**Fig. 4**) and XPS spectra (**Fig. 5**), hence the enhanced capacitance of CNPs/UCF supercapacitor is due to the combined electrochemical double layer and pseudo-*Faradic* charge storage. At higher current densities, the volume specific capacitance is found to reduce significantly and the variation is depicted in **Fig. 8D**. The volume specific and gravimetric energy densities of the CNPs/UCF supercapacitor is calculated at different current densities. A volume specific energy density of $0.753 \text{ mWh cm}^{-3}$ and a gravimetric energy density of 30 Wh kg^{-1} are achieved at a current density of 2.77 mA cm^{-2} . The variations in the volume specific and gravimetric energy densities with respect to the current densities are shown in **Fig. 8E** and **F**, respectively. Similarly, the volume specific and gravimetric power densities are calculated at different current densities and the same behavior is observed as that for the energy densities. A volume specific power density of 792 mW cm^{-3} is achieved by the CNPs/UCF supercapacitor at a current density of 16.66 mA cm^{-2} . Similarly, a high gravimetric power density of 32 kW kg^{-1} is achieved at a current density of 16.66 mA cm^{-2} and this value is comparable to that of the other carbon nanomaterials based supercapacitors reported. The hierarchically mesoporous CNPs/UCF hybrid electrodes possess unique three dimensional open mesoporous structure, which helps in the faster ion diffusion and hence predominantly enhanced charge storage is achieved. As the average pore-size of CNPs/UCF hybrid electrodes is 4.2 nm , the mesoporous CNPs/UCF electrodes undergo faster charging/discharging with high reversibility and hence high energy and power densities are achieved. The supercapacitive performance of the CNPs/UCF hybrid electrodes is comparable to that of the supercapacitors synthesized with CNTs and graphene based electrodes. It can be say that the novel method of preparing CNPs/UCF electrode-cum-current collectors is also responsible for the superior electrochemical performance.

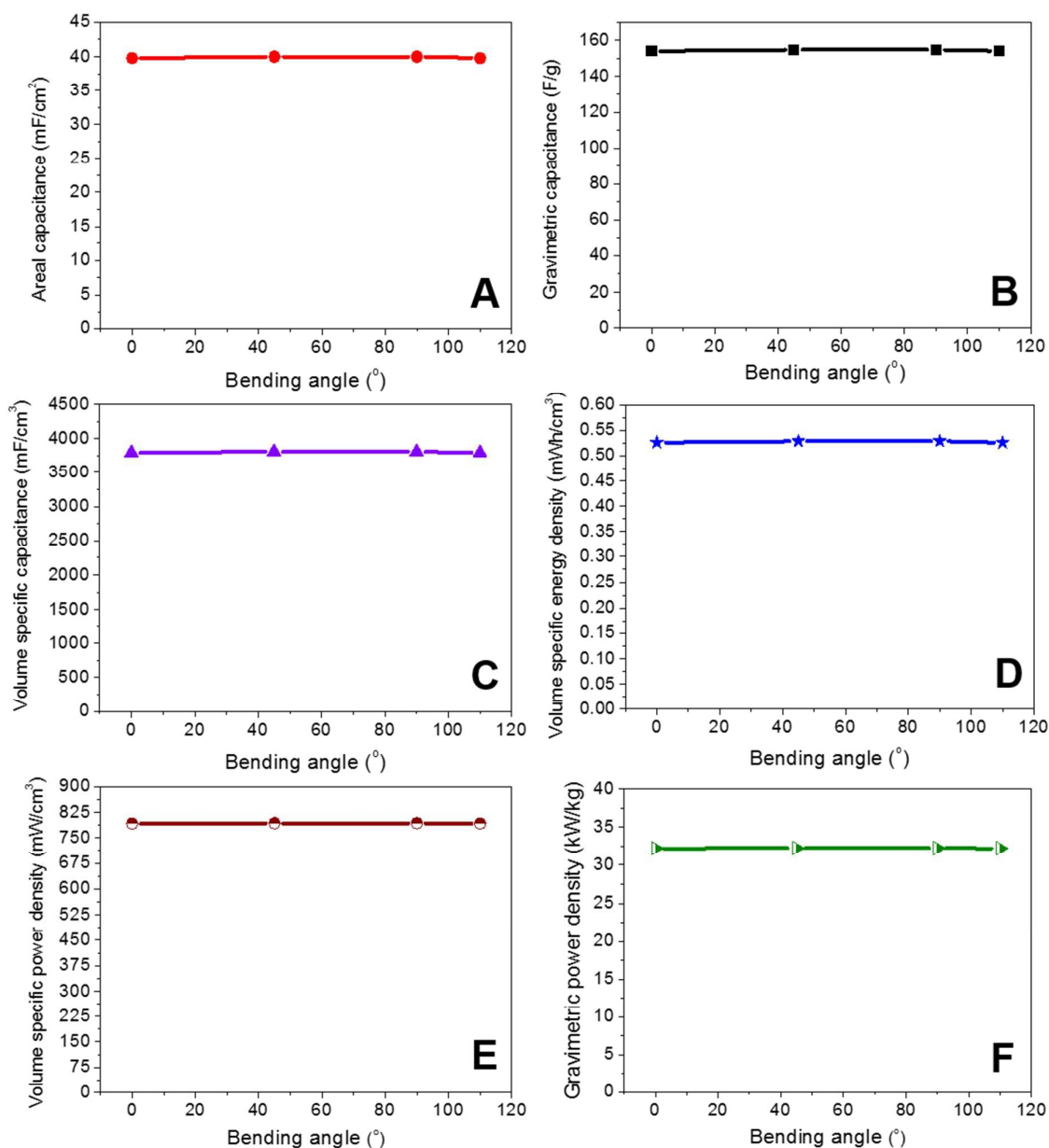


Fig. 9. Plots of variations in areal capacitance (A), gravimetric capacitance (B), volume specific capacitance (C), volume specific energy density (D), volume specific power density (E), and gravimetric power density (F) at different bending angles of the CNPs/UCF supercapacitor cell.

Nowadays, flexible supercapacitors are attaining much importance as these can be integrated with the upcoming flexible electronic devices. In order to examine the flexibility of the CNPs/UCF supercapacitor, galvanostatic charge/discharge measurements have been

carried out by bending the supercapacitor at various angles. The two-electrode cell set-up used for the study is shown in **Figure S5**. The CNPs/UCF supercapacitor was bent at different angles such as 0, 45, 90, and 110°. The galvanostatic charge/discharge measurements of the CNPs/UCF supercapacitor are carried out at different bending angles at a constant current density of 16.66 mA cm⁻² and the corresponding charge/discharge curves are shown in **Fig. 7F**. The digital images of the CNPs/UCF supercapacitor bent at various angles is shown in the inset of **Fig. 7F**. The highly symmetric galvanostatic charge/discharge curves represent the ideal capacitive behaviour of CNPs/UCF supercapacitor. From **Fig. 7F**, it is clear that there is no significant variation in the charge/discharge profiles of the CNPs/UCF supercapacitor while bending from its straight position (i.e., 0°) towards 110°. An areal capacitance of 39.8 mF cm⁻² is achieved at its 0° (straight) and this value is found to be constant until a bending of 110°. The areal capacitance variation with respect to different bending angles is shown in **Fig. 9A**. The percentage retention of the areal capacitance at different bending angles is shown in **Figure S6**. A gravimetric capacitance of 154 F/g is found to remain constant even at a supercapacitor bending of 110° and the variation in the gravimetric capacitance with respect to different bending angles is plotted in **Fig. 9B**. The percentage retention in the gravimetric capacitance at different supercapacitor bending angles is calculated and given in **Figure S7**. A volume specific capacitance of 3793 mF cm⁻³ is achieved even at a bending angle of 110° and the variation in the volume specific capacitance with respect to supercapacitor bending is depicted in **Fig. 9C**. Similar variations are observed in the case of volumetric capacitance also (**Figure S8**). The percentage retentions in the volumetric capacitance and volume specific capacitance are calculated at different bending angles and are shown in **Figure S9**. The volume specific energy density is calculated at different bending angles and is depicted in **Fig. 9D**. From this figure, it can be seen that the volume specific energy density (0.526 mWh cm⁻³) is unaltered even at a bending of 110°.

Similar variations are observed in the case of gravimetric energy density also (**Figure S10**). The percentage retention in the volume specific and gravimetric energy densities at different bending angles are plotted in **Figure S11**. The volume specific power densities and the gravimetric power densities are calculated at different bending angles and the variations are shown in **Fig. 9E** and **F**, respectively. A high volume specific power density of 792 mW cm^{-3} is achieved by the CNPs/UCF supercapacitor and this value is high when the CFs based flexible supercapacitors are considered.^{39,40,59} A high gravimetric power density of 32 kW/kg is achieved even at a supercapacitor bending angle of 110° . The percentage retentions in the volume specific and gravimetric power densities at different bending angles are calculated and are given in **Figure S12**. As there is no significant variation in the galvanostatic charge/discharge curves even at a bending angle of 110° , we can say that the CNPs/UCF supercapacitor is highly bendable and it is comparable to that of various flexible supercapacitors reported so far.^{34,60,61} The electrolyte leakage during the supercapacitor bending can be prevented by using sophisticated supercapacitor sealing procedures and leak-free supercapacitors can be developed by using solid-state polymer-based electrolytes.^{62,63}

Cycle life of a supercapacitor is a very important parameter, which figures out the active functioning of the supercapacitor electrodes over a period of time without undergoing any degradation. The cost factor is associated with the cycle life of the supercapacitor along with other performance parameters hence supercapacitors with long cycle life is preferred for their potential marketing. In order to estimate the cycle life of CNPs/UCF supercapacitor, galvanostatic charge/discharge measurement has been carried out for 28900 charge/discharge cycles at a constant current density of 16.66 mA cm^{-2} . The CNPs/UCF supercapacitor fabricated with electrodes with a CNPs loading density of $258 \mu\text{g cm}^{-2}$ is used for the galvanostatic charge/discharge cycling study. The volumetric capacitance of CNPs/UCF supercapacitor at various charge/discharge cycle numbers is shown in **Fig. 10A**. From **Fig.**

10A, it is clear that the volumetric capacitance is showing a repetitive increasing and decreasing trend during the cycling. A rise in the volumetric capacitance can be seen from its 8044th cycle till 10544th cycle with an increment of 228% of its initial value (it is denominated as ‘stage-I’ in **Fig. 10A**) and a decrease in the capacitance is observed then after. But soon after completing its 16544 cycles, the capacitance is found to increase again (it is denominated as ‘stage-II’ in **Fig. 10A**) and it is decreased to a value of 1336 mF cm⁻³ at its 19544th cycle. A rise in the capacitance is also observed at the third time from its 24544th towards 28900th cycle (it is denominated as ‘stage-III’ in **Fig. 10A**). Similar trend is also observed in the case of areal capacitance (**Fig. 10B**), volume specific capacitance (**Fig. 10C**), and gravimetric capacitance (**Fig. 10D**). From **Fig. 10B**, an increase in the areal capacitance can be seen at 10544th cycle (90 mF cm⁻²) and it is found to reduce significantly thereafter. A volume specific capacitance of 8650 mF cm⁻³) is achieved at 10544th cycle whereas only 6349 mF cm⁻³ is retained after 28900 cycles (**Fig. 10C**). A two-fold increase in the gravimetric capacitance is observed soon after the completion of 10544th cycle and a nearly high value of 258 F g⁻¹ is observed at the end of 28900th cycle (**Fig. 10D**). The repetitive increase and decrease in the capacitance of the supercapacitors during the continuous charge/discharge cycling test is reported in various literatures⁶⁴⁻⁷⁰ but no explanation to such a phenomena is given. The repetitive increase and decrease of capacitance of the supercapacitor during its cycling may not be due to a single reason but there can be many reasons. The electrochemical behaviour of the supercapacitor at a specific cycle number is dependent on (i) the equivalent series resistance of the system, (ii) the pore structure of the electrode, (iii) the number of opened pores within the electrode, (iv) the effective surface area of the electrode available for the charge storage without any wreckage, (v) the changes occurred in the surface functionalities during charging/discharging if the electro-active material consisting of surface groups adhered to it, etc. The increase or decrease in the

capacitance at a given cycle number is due to the interplay between the above mentioned factors. But it is very difficult to figure-out the specific reason since two or more factors may be simultaneously governing the net electrochemical behaviour of the supercapacitor electrode at a particular cycle number. In the present study, we propose mechanisms, which are responsible for the repetitive increase and decrease of the capacitances of CNPs/UCF supercapacitor as follows.

According to the proposed mechanisms, the repetitive increase and decrease of the capacitances is due to the unique, hierarchically mesoporous three dimensional structure of the CNPs in the CNPs/UCF hybrid electrodes. This phenomena can be explained with the help of some hypotheses about the ion diffusion mechanisms through the hierarchically mesoporous carbon monolayers of the CNPs. As aforementioned, CNP is consisting of a porous architecture in which the thickness of CNPs at its central region is higher than that of their edges [evident from TEM images (**Fig. 2E-F**)]. The central canal of the three dimensional CNP constitutes a large number of mesoporous carbon monolayers. Although the CNP is having a three dimensional structure, but it is schematically represented as two-dimensional in **Fig. 11A**. The portion from the central canal of the CNPs towards its outer surface is schematically shown in **Fig. 11B - E**. As discussed above, the capacitance of CNPs/UCF supercapacitor is the sum of double layer and pseudo-*Faradic* capacitances. During the initial stages of charge/discharge cycles, there could be a certain number of pores available for the ion diffusion within the three dimensional network of CNP, which is schematically shown in **Fig. 11B**. Some of the pores may not be available for the ion diffusion due to pore blockade and the blocked pores are represented as yellow circles in **Fig. 11B**. Depending on the wettability of the electrolyte at the outer surfaces of the CNPs, the oxygen-containing surface functional groups are activated, which leads to an enhanced capacitance. At stage-I, the electrolyte wettability towards the inner layers are increased due

to the opening of pores on the outer surfaces of the CNP and as a result, an increase in the capacitance is observed and the mechanism is schematically represented in **Fig. 11C**. Hence the reason for the increase in capacitance at stage-I is due to the activation of surface functional groups on the outer surfaces of CNPs. But soon after this, the capacitance is found to decrease gradually and it is possibly due to the increase in internal resistance. The diffusion of electrolyte ion towards the interior regions of the CNPs can be expected over a period of time. At stage-II, there could be more number of pores opened in the mid-region of the CNP (as shown in **Fig. 11D**), which can trigger faster ion diffusion and as a result, a rise in the capacitance is observed. But this increment is small when compared the one occurred during stage-I. Due to the thickness of CNP in the central canal, the electrolyte ions may not be able to wet the surfaces of central canal within a short period of time. But as the charge/discharge process is continuing, there can be the movement of the ions towards the central canal. Hence at stage-III, the increase in capacitance is directly contributed by the double layer charges since the central canal of the CNP is wet with the electrolyte ions and it is schematically shown in **Fig. 11E**. A volume specific energy density of $0.526 \text{ mWh cm}^{-3}$ is increased two-fold (1.2 mWh cm^{-3}) after completing 10544 cycles and the variation of the volume specific energy density during the cycling test is shown in **Fig. 10E**. **Fig. 10F** represents the galvanostatic charge/discharge curves of the CNPs/UCF supercapacitor just before the completion of 28900 cycles, which shows highly symmetric charge/discharge cycles with good linear voltage-time profiles. From **Fig. 10**, it is clear that the CNPs/UCF supercapacitor exhibits super-long cycling stability by performing 28900 cycles. From the galvanostatic charge/discharge cycling study, it can be say that the performance of CNPs/UCF supercapacitor is much comparable or better in terms of super-long cycling stability when compared to that of other supercapacitors reported earlier.^{34,39,40,59-61} Since the CNPs/UCF hybrid electrodes exhibit high specific surface area, good electronic conductivity,

and high chemical stability, it can be a potential candidate for use in energy conversion devices too.

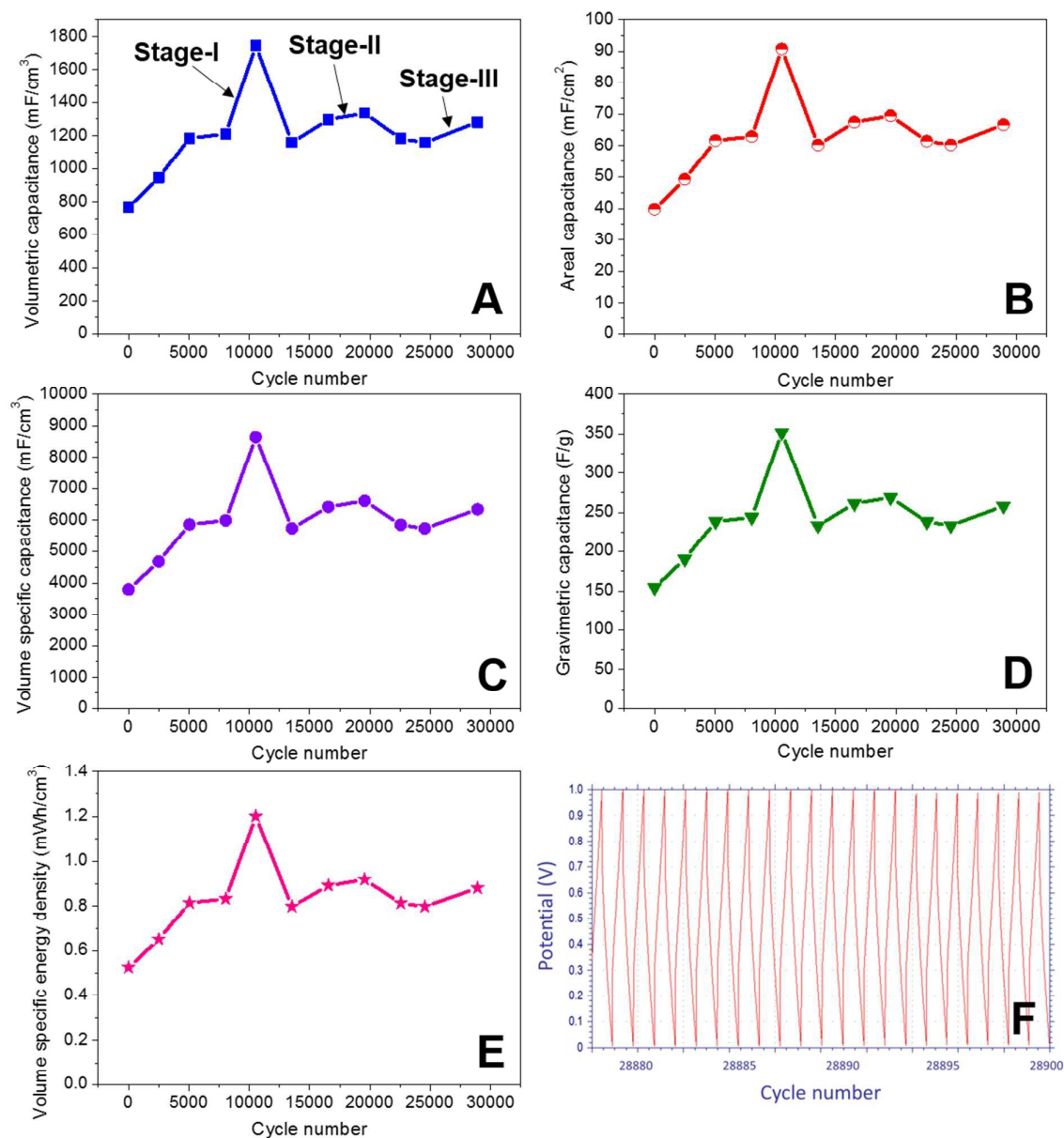


Fig. 10. Plots of variations in volumetric capacitance (A), areal capacitance (B), volume specific capacitance (C), gravimetric capacitance (D), and volume specific energy density (E) at different cycling numbers for the CNPs/UCF supercapacitor; Galvanostatic charge/discharge cycles just before completing its 28900th cycle for the CNPs/UCF supercapacitor (F).

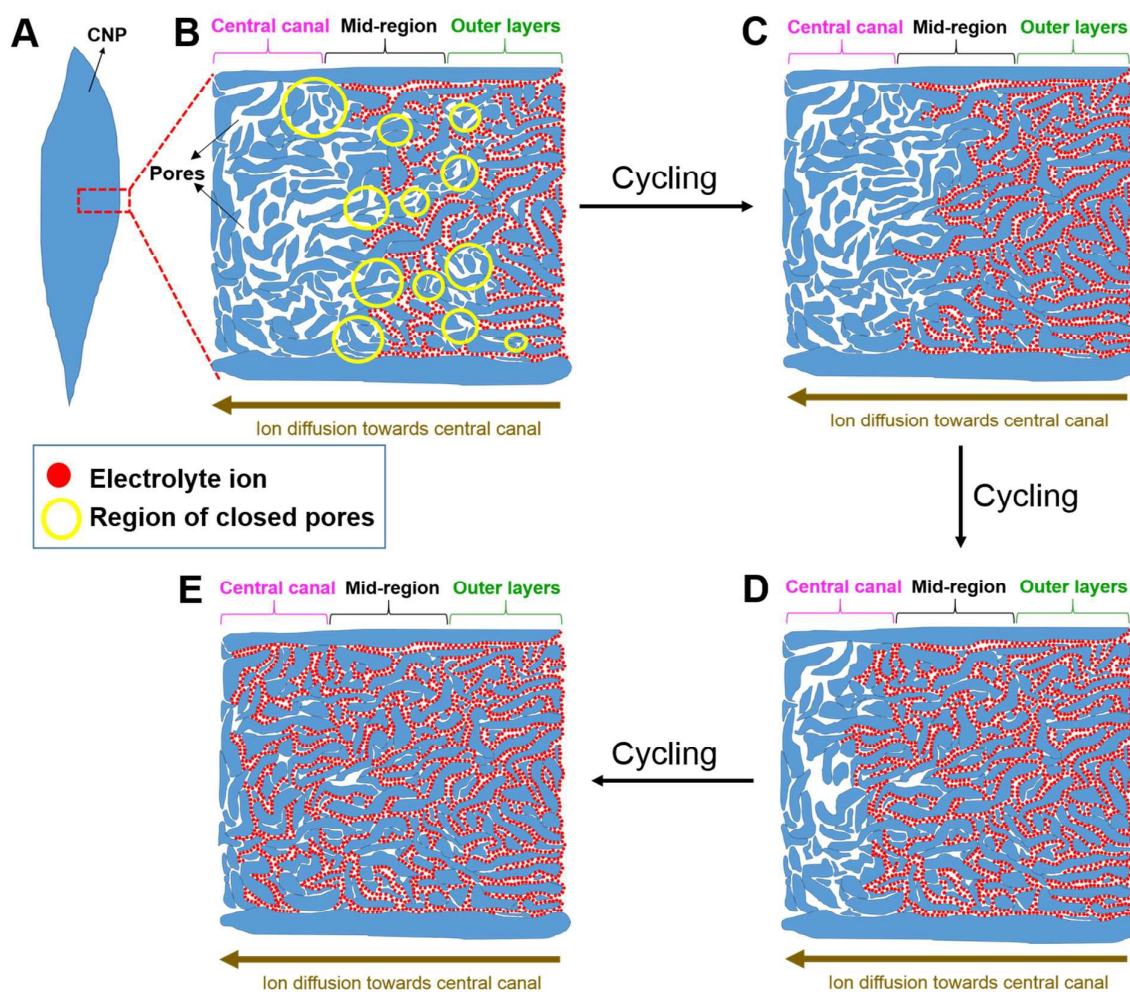


Fig. 11. Schematic showing the ion diffusion mechanisms through the hierarchically mesoporous CNP at prolonged galvanostatic charge/discharge cycling the CNPs/UCF supercapacitor. (A) Schematic showing a CNP; Ion diffusion through CNP at early stages of cycling (B), at stage-I (C), at stage-II (D), and at stage-III (E).

4. Conclusions

Hierarchically mesoporous CNPs were synthesized on UCF by CVD. A highly flexible supercapacitor was fabricated with CNPs/UCF electrode-cum-current collectors and no other separate current collectors were used. The mesoporous architecture of CNPs/UCF hybrid electrodes has triggered the rapid ion diffusion processes during its operation and an enhanced supercapacitor performance is notified. The bendability of the supercapacitor was

tested by galvanostatic charge/discharge measurements by bending the CNPs/UCF supercapacitor at different angles and no significant change was observed even at a bend of 110° . The highly flexible CNPs/UCF supercapacitor exhibits a high gravimetric capacitance of 154 F g^{-1} with a high gravimetric power density of 32 kW kg^{-1} . The reasons for the superior electrochemical performance of the CNPs/UCF supercapacitor are the possession of mesoporous electrode architecture as well as the presence of oxygen-containing surface functional groups on the CNPs/UCF hybrids. The CNPs/UCF supercapacitor has achieved a super-long cyclic stability of more than 28900 cycles. The present study proclaims the development of novel CNPs/UCF electrode-cum-current collectors for flexible supercapacitors and can also be used for other electrochemical devices too.

Acknowledgements

This work was supported by the Department of Science and Technology, India. The authors acknowledge Dr Malay K. Das, Department of Mechanical Engineering, Indian Institute of Technology Kanpur, India for providing the experimental facility for this work.

Notes and references

1. L. Sun, C. Tian, M. Li, X. Meng, L. Wang, R. Wang, J. Yin and H. Fu, *J. Mater. Chem. A*, 2013, 1, 6462.
2. M. M. Shaijumon, F. S. Ou, L. Ci and P. M. Ajayan, *Chem. Commun.*, 2008, 2373.
3. X. Fan, H. Zhou and X. Guo, *RSC Adv.*, 2015, 5, 45484.
4. Y. Yoo, S. Kim, B. Kim and W. Kim, *J. Mater. Chem. A*, 2015, 3, 11801.
5. S. He and W. Chen, *Nanoscale*, 2015, 7, 6957.
6. Y. Shao, M. F. El-Kady, L. J. Wang, Q. Zhang, Y. Li, H. Wang, M. F. Mousavi and R. B. Kaner, *Chem. Soc. Rev.*, 2015, 44, 3639.
7. P. Agnihotri, S. Basu, and K. K. Kar, *Carbon*, 2011, 49, 3098.
8. Y. B. Tan and J. M. Lee, *J. Mater. Chem. A*, 2013, 1, 14814.

9. Y. Gao, Y. S. Zhou, M. Qian, H. M. Li, J. Redepenning, L. S. Fan, X. N. He, W. Xiong, X. Huang, M. M. Samani, L. Jiang and Y. F. Lu, *RSC Adv.*, 2013, 3, 20613.
10. C. Dong, Y. Wang, J. Xu, G. Cheng, W. Yang, T. Kou, Z. Zhang and Y. Ding, *J. Mater. Chem. A*, 2014, 2, 18229.
11. J. Zang and X. Li, *J. Mater. Chem.*, 2011, 21, 10965.
12. K. K. Kar, J. K. Pandey and S. K. Rana, *Handbook of Polymer Nanocomposites: Processing, performance and Applications*, Springer, Germany, 2015, ch. 19, pp. 480-504.
13. S. Park, M. Vosguerichian and Z. Bao, *Nanoscale*, 2013, 5, 1727.
14. L. Hu and Y. Cui, *Energy Environ. Sci.*, 2012, 5, 6423.
15. Y. He, W. Chen, C. Gao, J. Zhou, X. Li and E. Xie, *Nanoscale*, 2013, 5, 8799.
16. L. Dai, D. W. Chang, J. B. Baek and W. Lu, *Small*, 2012, 8, 1130.
17. K. Novoselov, V. Fal, L. Colombo, P. Gellert, M. Schwab and K. Kim, *Nature*, 2012, 490, 192.
18. S. Bose, T. Kuila, A. K. Mishra, R. Rajasekar, N. H. Kim and J. H. Lee, *J. Mater. Chem.*, 2012, 22, 767.
19. H. Jiang, P. S. Lee and C. Li, *Energy Environ. Sci.*, 2013, 6, 41.
20. M. Kaempgen, C. K. Chan, J. Ma, Y. Cui and G. Gruner, *Nano Lett.*, 2009, 9, 1872.
21. L. Hu, M. Pasta, F. L. Mantia, L. Cui, S. Jeong, H. D. Deshazer, J. W. Choi, S. M. Han and Y. Cui, *Nano Lett.*, 2010, 10, 708.
22. Y. J. Kang, H. Chung, C.-H. Han and W. Kim, *Nanotechnology*, 2012, 23, 065401.
23. Y. J. Kang, S.-J. Chun, S.-S. Lee, B.-Y. Kim, J. H. Kim, H. Chung, S.-Y. Lee and W. Kim, *ACS Nano*, 2012, 6, 6400.
24. V. L. Pushparaj, M. M. Shaijumon, A. Kumar, S. Murugesan, L. Ci, R. Vajtai, R. J. Linhardt, O. Nalamasu and P. M. Ajayan, *Proc. Natl. Acad. Sci. U. S. A.*, 2007, 104, 13574.
25. C. Huang and P. S. Grant, *Sci. Rep.*, 2013, 3, 2393.

26. A. R. Boccaccini, J. Cho, J. A. Roether, B. J. C. Thomas, E. J. Minay, M. S. P. Shaffer, *Carbon*, 2006, 44, 3149.
27. H. Zhang, G. Cao, W. Wang, K. Yuan, B. Xu, W. Zhang, J. Cheng, Y. Yang, *Electrochim. Acta*, 2009, 54, 1153.
28. C. Peng, S. Zhang, D. Jewell, G. Z. Chen, *Prog. Nat. Sci.*, 2008, 18, 777.
29. Z. J. Han, D. H. Seo, S. Yick, J. H. Chen and K. K. Ostrikov, *NPG Asia Mater.*, 2014, 6, e140.
30. T. Chen, H. Peng, M. Durstock and L. Dai, *Sci. Rep.*, 2014, 4, 3612.
31. L. Hu, M. Pasta, F. L. Mantia, L. Cui, S. Jeong, H. D. Deshazer, J. W. Choi, S. M. Han and Y. Cui, *Nano Lett.*, 2010, 10, 708.
32. L. Bao and X. Li, *Adv. Mater.*, 2012, 24, 3246.
33. W.-W. Liu, X.-B. Yan, J.-W. Lang, C. Peng and Q.-J. Xue, *J. Mater. Chem.*, 2012, 22, 17245.
34. J. Bae, M. K. Song, Y. J. Park, J. M. Kim, M. Liu and Z. L. Wang, *Angew. Chem., Int. Ed.*, 2011, 50, 1683.
35. Y. Fu, X. Cai, H. Wu, Z. Lv, S. Hou, M. Peng, X. Yu and D. Zou, *Adv. Mater.*, 2012, 24, 5713.
36. X. Xiao, T. Li, P. Yang, Y. Gao, H. Jin, W. Ni, W. Zhan, X. Zhang, Y. Cao and J. Zhong, *ACS Nano*, 2012, 6, 9200.
37. J. Ren, L. Li, C. Chen, X. Chen, Z. Cai, L. Qiu, Y. Wang, X. Zhu and H. Peng, *Adv. Mater.*, 2013, 25, 1155.
38. Y. Meng, Y. Zhao, C. Hu, H. Cheng, Y. Hu, Z. Zhang, G. Shi and L. Qu, *Adv. Mater.*, 2013, 25, 2326.

39. X. Xiao, T. Li, P. Yang, Y. Gao, H. Jin, W. Ni, W. Zhan, X. Zhang, Y. Cao, J. Zhong, L. Gong, W.-C. Yen, W. Mai, J. Chen, K. Huo, Y.-L. Chueh, Z. L. Wang and J. Zhou, *ACS Nano*, 2012, 6, 9200.
40. V. T. Le, H. Kim, A. Ghosh, J. Kim, J. Chang, Q. A. Vu, D. T. Pham, J.-H. Lee, S.-W. Kim and Y. H. Lee, *ACS Nano*, 2013, 7, 5940.
41. K. K. Kar and D. Sathiyamoorthy, *J. Mater. Process. Technol.*, 2009, 209, 3022.
42. Z. Ma, X. Zhao, C. Gong, J. Zhang, J. Zhang, X. Gu, L. Tong, J. Zhou and Z. Zhang, *J. Mater. Chem. A*, 2015, 3, 13445.
43. T. Szabo, O. Berkesi and I. Dekany, *Carbon*, 2005, 43, 3186.
44. C. Hontoria-Lucas, A. J. Lopez-Peinado, J. D. Lopez-Gonzalez, M. L. Rojas-Cervantes and R. M. Martin-Aranda, *Carbon*, 1995, 33, 1585.
45. P. C. Wong, Y. S. Li and K. A. R. Mitchell, *Appl. Surf. Sci.*, 1995, 84, 245.
46. R. W. Paynter, *Surf. Interface Anal.*, 1998, 26, 674.
47. T. Ishizaki, S. Chiba, Y. Kaneko and G. Panomsuwan, *J. Mater. Chem. A*, 2014, 2, 10589.
48. J. Diaz, G. Paolicelli, S. Ferrer and F. Comin, *Phys. Rev. B*, 1996, 54, 8064.
49. R. Haerle, E. Riedo, A. Pasquarello and A. Baldereschi, *Phys. Rev. B*, 2002, 65, 45101.
50. M. Seredych, D. Hulicova-Jurcakova, G. Q. Lu and T. J. Bandoz, *Carbon*, 2008, 46, 1475.
51. J. R. Pels, F. Kapteijn, J. A. Moulijn, Q. Zhu and K. M. Thomas, *Carbon*, 1995, 33, 1641.
52. S. Brunauer, L. S. Deming, W. E. Deming and E. Teller, *J. Am. Chem. Soc.*, 1940, 62, 1723.
53. G. Zhang, L. Ren, Z. Yan, L. Kang, Z. Lei, H. Xu, F. Shi and Z.-H. Liu, *J. Mater. Chem. A*, 2015, 3, 14567.
54. Z. Yu, L. Tetard, L. Zhai and J. Thomas, *Energy Environ. Sci.*, 2015, 8, 702.
55. J. Zhi, Y. Wang, S. Deng and A. Hu, *RSC Adv.*, 2014, 4, 40296.

56. L. Zhang and G. Shi, *J. Phys. Chem. C*, 2011, 115, 17206.
57. M. A. Montes-Moran, D. Suarez, J. A. Menendez and E. Fuente, *Carbon*, 2004, 42, 1219.
58. C. A. Leon y Leon and L. R. Radovic, *Interfacial Chemistry and Electrochemistry of Carbon Surfaces*, Marcel Dekker, New York, Vol. 24, 1994, p. 213.
59. P. Yang, X. Xiao, Y. Li, Y. Ding, P. Qiang, X. Tan, W. Mai, Z. Lin, W. Wu, T. Li, H. Jin, P. Liu, J. Zhou, C. P. Wong and Z. L. Wang, *ACS Nano*, 2013, 7, 2617.
60. K. Wang, Q. Meng, Y. Zhang, Z. Wei and M. Miao, *Adv. Mater.*, 2013, 25, 1494.
61. J. Tao, N. Liu, W. Ma, L. Ding, L. Li, J. Su and Y. Gao, *Sci. Rep.*, 2013, 3, 1.
62. Q. F. Wang, X. F. Wang, B. Liu, G. Yu, X. J. Hou, D. Chen and G. Z. Shen, *J. Mater. Chem. A*, 2013, 1, 2468.
63. X. D. Zhang, Z. Y. Lin, B. Chen, S. Sharma, C. P. Wong, W. Zhang and Y. L. Deng, *J. Mater. Chem. A*, 2013, 1, 5835.
64. Q. Cheng, J. Tang, J. Ma, H. Zhang, N. Shinya and L.-C. Qin, *Phys. Chem. Chem. Phys.*, 2011, 13, 17615.
65. L. Chang, W. Wei, K. Sun and Y. H. Hu, *J. Mater. Chem. A*, 2015, 3, 10183.
66. C. O. Ania, V. Khomenko, E. Raymundo-Pinero, J. B. Parra and F. Beguin, *Adv. Funct. Mater.*, 2007, 17, 1828.
67. H. Jiang, J. Ma and C. Li, *Chem. Commun.*, 2012, 48, 4465.
68. Y. Yu, W. Gao, Z. Shen, Q. Zheng, H. Wu, X. Wang, W. Song and K. Ding, *J. Mater. Chem. A*, 2015, 3, 16633.
69. L. Zhang and G. Shi, *J. Phys. Chem. C*, 2011, 115, 17206.
70. J. Hou, C. Cao, X. Ma, F. Idrees, B. Xu, X. Hao and W. Lin, *Sci. Rep.*, 2014, 4, 7260.

Table of Contents

Flexible supercapacitor manufactured with hierarchically mesoporous carbon nanopetals based electrodes exhibit high capacitance and power density with super-long cyclic stability.

